

The Antesonic Condition for the Explosion of Core-Collapse Supernovae II: Rotation and Turbulence

Matthias J. Raives^{1,2}, Todd A. Thompson^{1,2}, & Sean M. Couch^{3,4,5,6}

¹*Department of Astronomy, The Ohio State University, Columbus, OH 43210, USA*

²*Center for Cosmology and Astroparticle Physics, The Ohio State University, Columbus, OH 43210, USA*

³*Department of Physics and Astronomy, Michigan State University, East Lansing, MI 48824, USA*

⁴*Department of Computational Mathematics, Science, and Engineering, Michigan State University, East Lansing, MI 48824, USA*

⁵*National Superconducting Cyclotron Laboratory, Michigan State University, East Lansing, MI 48824, USA*

⁶*Joint Institute for Nuclear Astrophysics-Center for the Evolution of the Elements, Michigan State University, East Lansing, MI 48824, USA*

25 February 2022

ABSTRACT

In the problem of steady free-fall onto a standing shockwave around a central mass, the “antesonic” condition limits the regime of stable accretion to $c_T^2/v_{\text{esc}}^2 \leq 3/16$, where c_T is the isothermal sound speed in the subsonic post-shock flow, and v_{esc} is the escape velocity at the shock radius. Above this limit, it is impossible to satisfy both the Euler equation and the shock jump conditions, and the system transitions to a wind. This physics explains the existence of a critical neutrino luminosity in steady-state models of accretion in the context of core-collapse supernovae. Here, we extend the antesonic condition to flows with rotation and turbulence using a simple one-dimensional formalism. Both effects decrease the critical post-shock sound speed required for explosion. While quite rapid rotation is required for a significant change to the critical condition, we show that the level of turbulence typically achieved in supernova simulations can greatly impact the critical value of c_T^2/v_{esc}^2 . A core angular velocity corresponding to a millisecond rotation period after contraction of the proto-neutron star results in only a ~ 5 per-cent reduction of the critical curve. In contrast, near-sonic turbulence with specific turbulent kinetic energy $K/c_T^2 = 0.5 - 1$, leads to a decrease in the critical value of c_T^2/v_{esc}^2 by $\sim 20 - 40$ per-cent. This analysis provides a framework for understanding the role of post-shock turbulence in instigating explosions in models that would otherwise fail and helps explain why multi-dimensional simulations explode more easily than their one-dimensional counterparts.

Key words: accretion – hydrodynamics – shock waves – supernovae: general

1 INTRODUCTION

A core-collapse supernova is initiated when the iron core of a massive star begins to collapse under its own gravity, beginning a runaway accretion process that is only halted when the core reaches nuclear density. The sudden stiffening of the equation of state launches a shock wave into the accreting fluid, which loses energy as it moves outward, eventually stalling at a radius of a few hundred kilometers. The central problem in supernova theory is explaining under what conditions, and by what mechanism, the shock is revived to produce a successful supernova.

Burrows & Goshy (1993) quantitatively explored the concept of the critical condition for explosion. They showed that a spherically-symmetric accretion flow onto a standing accretion shock, subject to optically thin neutrino heating and cooling, only has a steady-state solution below a critical core neutrino luminosity $L_{\nu,\text{crit}}$, which is a function of

the mass accretion rate \dot{M} , as well as the proto-neutron star (PNS) mass M and radius R . Since then, numerical studies of the critical condition in time-dependent simulations have shown that the critical neutrino luminosity at a given \dot{M} is generally lower in 2D (axisymmetry) and 3D than in 1D (spherical symmetry) (Murphy & Burrows 2008; Murphy & Dolence 2017), though higher in 3D than in 2D (Couch 2013a; Takiwaki et al. 2014). Other simulations have investigated the critical curve with rotation (Iwakami et al. 2014), finding that rotation can drive a model to explosion even if the neutrino luminosity is below the “critical” value suggested by non-rotating simulations (Yamasaki & Yamada 2005). Work has also been done on explosion criteria that more directly ties the success or failure of explosion in simulations to characteristics of the progenitor models (Ugliano et al. 2012; Pejcha & Thompson 2015; Sukhbold et al. 2016),

including the core compactness (O’Connor & Ott 2011) and the M_4 mass (Ertl et al. 2016).

Pejcha & Thompson (2012) showed that a critical condition similar to that of Burrows & Goshy (1993) can be derived for an isothermal equation of state in the post-shock accretion flow, where the ratio of the isothermal sound speed c_T to the escape velocity at the shock is the controlling parameter. Above a critical value of $c_T^2/v_{\text{esc}}^2 = 3/16$, it is impossible to simultaneously satisfy the time-steady Euler equations and the shock-jump conditions (see §2). Pejcha & Thompson (2012) also showed that this physics determines the critical condition in the more complete problem of Burrows & Goshy (1993), and that the antesonic condition is not identical to the heuristic condition that the timescale for advection of matter through the gain region $\tau_{\text{advection}}$ equals the heating timescale τ_{heating} (e.g., Thompson et al. 2004). Pejcha & Thompson (2012) hypothesized that, in a time-dependent simulation, an accretion flow that exceeded the antesonic condition would dynamically transition to a thermally-driven wind. This predicted behavior was verified in time-dependent simulations by Gabay et al. (2015); Raives et al. (2018).

The applicability of the antesonic condition to the less idealized accretion flows present in full-physics multi-dimensional simulations of core-collapse supernovae with turbulence, convection, and other instabilities is unclear. In this paper, we take a step toward that understanding by deriving the antesonic condition for the idealized isothermal post-shock model flow with 1D prescriptions for turbulence and rotation. Importantly, our analysis shows that the critical condition is significantly affected by the near-sonic turbulence that occurs generically in multi-dimensional simulations, and thus provides a way to interpret many previous results. In contrast, in our model problem relatively extreme rotation rates producing millisecond rotation periods for the fully-contracted neutron star are required for the critical condition to be affected during the stalled-shock phase.

While previous works have investigated the effects of rotation (Yamasaki & Yamada 2005) and turbulence (Yamasaki & Yamada 2007; Mabanta & Murphy 2018; Couch et al. 2020) on the critical curve, here we are able to provide an analytic criterion for explosion that can be used to understand why some simulations explode, while others fail. We explicitly show how rotation and turbulence decrease the critical post-shock sound speed required for explosion. In §2, we present the isothermal derivation from Pejcha & Thompson (2012). We then add rotation (§2.1), both isotropic and anisotropic turbulence (§2.2), and discuss a generalized critical condition allowing for rotation and turbulence (§2.3). In §3, we propose a framework for understanding further generalizations to the antesonic condition (§3.1), as well as a comparison to both parameterized 1D (§3.2) and full-physics, multi-dimensional simulations (§3.3).

2 THE ANTESONIC CONDITION

For context, we derive the simplest form of the antesonic condition, following Pejcha & Thompson (2012). An isothermal fluid undergoing steady-state shocked accretion in a point-mass gravitational potential must simultaneously sat-

isfy both the Euler equations,

$$\frac{1}{\rho} \frac{d\rho}{dr} = -\frac{2}{r} - \frac{1}{v_r} \frac{dv_r}{dr} \quad (1)$$

$$v_r \frac{dv_r}{dr} = -\frac{1}{\rho} \frac{dP}{dr} - \frac{GM}{r^2}, \quad (2)$$

and the shock-jump conditions,

$$\rho_1 v_1 = \rho_2 v_2, \quad (3)$$

$$\rho_1 v_1^2 + P_1 = \rho_2 v_2^2 + P_2, \quad (4)$$

as well as an equation of state (EOS). For the purposes of this paper, we limit ourselves to an isothermal EOS of the form

$$P = c_T^2 \rho \quad (5)$$

in the post-shock fluid for simplicity. An exact antesonic condition can also be derived for a polytropic equation of state (Raives et al. 2018), and an antesonic condition also holds for more general equations of state with heating and cooling (Pejcha & Thompson 2012; Pejcha & Thompson 2015).

In spherical symmetry, the Euler equations assume the dimensionless form

$$\left(\mathcal{M} - \frac{1}{\mathcal{M}} \right) \frac{d\mathcal{M}}{d\xi_{\text{th}}} = \frac{2}{\xi_{\text{th}}} - \frac{1}{2\xi_{\text{th}}^2}, \quad (6)$$

where $\mathcal{M} = v_r/c_T$ is the Mach number of the fluid, and

$$\xi_{\text{th}} \equiv \frac{c_T^2 r}{2GM} = \frac{c_T^2}{v_{\text{esc}}^2} \quad (7)$$

is the thermal “antesonic” ratio, so named because this occurs at smaller r than the sonic point in the classic Parker wind problem. Although in previous papers (Pejcha & Thompson 2012; Pejcha & Thompson 2015; Raives et al. 2018), we referred to this quantity as simply the “antesonic ratio,” without qualification, in this paper we attach the “thermal” prefix to distinguish it from the similar dimensionless ratios that are important to the additional physics considered below.

Assuming the fluid above the shock is undergoing pressure-less free-fall ($P_2 = 0$, $v_2 = -\sqrt{2GM/r}$) onto the shock, the shock-jump conditions can be used to specify the fluid velocity immediately downstream of the shock as a function of the shock radius:

$$\mathcal{M}_1 = \frac{1}{2} \left(-\xi_{\text{th}}^{-1/2} + \sqrt{\xi_{\text{th}}^{-1} - 4} \right). \quad (8)$$

By substituting Equation (8) into Equation (6), we find the value (or values) of ξ_{th} (and thus, c_T) that corresponds to a solution where the velocity profile is tangent to the locus of all possible shock positions (as specified by Equation 8).

The importance of this solution is shown graphically in Figure 1. We integrated Equation (6) outward from the PNS surface $r_\nu = 30$ km (dotted line), for various sound speeds at fixed assumed value of $\dot{M} = 1 M_\odot/\text{s}$ (solid colored lines). Equation (8) for the shock-jump conditions is shown as the black dashed line. For small c_T , the accretion flows go from the PNS surface to the shock, where they transition to the pressure-less free-fall conditions assumed to derive the shock jump condition (for clarity, these upstream profiles are not shown). For high values of c_T (green to yellow), the accretion solutions do not intersect the shock conditions, indicating it is impossible to satisfy the time-steady Euler equation and

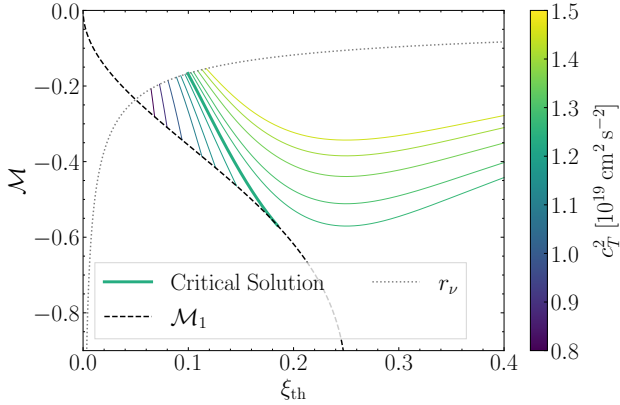


Figure 1. A graphical representation of the antesonic condition. Solutions to the Euler equations (solid lines) are specified by the sound speed c_T (increasing from left to right). They start at $r_\nu = 30$ km (dotted grey line) and continue until they satisfy the boundary conditions specified by the shock-jump conditions (Equation 8, black dashed line). Solutions with a sound speed larger than that of the critical solution (bolded; $\xi_{th} = 3/16$) never satisfy the shock-jump conditions, and are thus unphysical in this context because they cannot describe shocked accretion flow. The solutions pictured are for $\rho_\nu = 3 \times 10^{10} \text{ g cm}^{-3}$, $M = 1.4 M_\odot$, and $\dot{M} = 1 M_\odot/\text{s}$.

the shock-jump conditions simultaneously. The dark green line indicates the critical solution where the two curves are tangent to one another. For the pure isothermal case, the critical value of ξ_{th} is equal to (Pejcha & Thompson 2012)¹

$$\xi_{th,crit} = \frac{3}{16}. \quad (9)$$

For isothermal and polytropic fluids Pejcha & Thompson (2012); Raives et al. (2018), the critical value of ξ_{th} is always the maximum value of ξ_{th} anywhere in the accretion flow, and this maximum always occurs at the shock. However, this is not necessarily the case for other equations of state or when considering additional physics. As shown by Pejcha & Thompson (2012), for an equation of state that is coupled to neutrino heating and cooling, the maximum value of c_s^2/v_{esc}^2 occurs near the “gain radius,” where neutrino heating balances cooling in the post-shock flow.

2.1 Rotation

We first consider the case of a non-turbulent fluid rotating with velocity $v_\phi(r)$, which experiences a centrifugal acceleration in the equatorial plane:

$$a_{cen} = \frac{v_\phi^2}{r} = 2 \frac{GM}{r^2} \xi_{cen}, \quad (10)$$

where

$$\xi_{cen} \equiv \frac{v_\phi^2}{v_{esc}^2}, \quad (11)$$

so that Equation (2) becomes

$$v_r \frac{dv_r}{dr} = -\frac{1}{\rho} \frac{dP}{dr} - \frac{GM}{r^2} (1 - 2\xi_{cen}) \quad (12)$$

In dimensionless form, (for comparison with Equation (6)), we have

$$\left(\mathcal{M} - \frac{1}{\mathcal{M}} \right) \frac{d\mathcal{M}}{d\xi_{th}} = \frac{2}{\xi_{th}} - \frac{1 - 2\xi_{cen}}{2\xi_{th}^2}. \quad (13)$$

As the rotational velocity is the same on either side of the shock, the presence of rotation does not change the shock-jump conditions. Following the same procedure as for the non-rotating case (i.e., substituting Equation (8) into Equation (13)), we obtain the following expression for the critical antesonic ratio:

$$\xi_{th,crit} = \frac{1}{32} \left(3 - 16\xi_{cen,crit} + \sqrt{9 + 32\xi_{cen,crit}} \right). \quad (14)$$

In the limit $\xi_{cen,crit} \ll 1$, Equation (14) reduces to

$$\xi_{th,crit} + \frac{1}{3}\xi_{cen,crit} = \frac{3}{16}. \quad (15)$$

In the presence of rotation, there is not one single critical antesonic ratio but rather, the antesonic condition specifies a relation between the thermal and centrifugal terms at the shock that defines the critical solution.

We follow the same procedure used to generate Figure 1 to find the critical value of c_T for many different assumed values of \dot{M} . For each \dot{M} , we search for the tangent of the flow profiles obtained from Equation (13) with the shock jump conditions. Because the value of the shock radius at the critical value of c_T changes for each \dot{M} , the mapping between the antesonic condition given in Equation (9) or Equation (14) and \dot{M} is not trivial. We then plot this “critical curve” showing the critical value of c_T as a function of \dot{M} in Figure 2². In order to integrate Equation (13) and construct Figure 2, we assume a rotation profile $v_\phi(r)$ corresponding to angular momentum conservation with $v_\phi \propto r^{-1}$. We have also tested the case of a solid body rotation profile ($v_\phi \propto r$) (see below).

By allowing a second parameter to vary (in this case, the core rotation rate Ω) we form a 2D critical surface (e.g., as in Iwakami et al. 2014). For clarity, we show individual slices of the critical surface at fixed values of Ω . For aid in interpreting the figure, we normalize the rotation rates by

$$\Omega_{ms} = \frac{2\pi}{1 \text{ ms}} \left(\frac{10 \text{ km}}{r_\nu} \right)^2, \quad (16)$$

the rotation rate that would lead to a neutron star with a period of 1 ms after the PNS cools and contracts to a radius of 10 km, assuming the angular momentum of the PNS is conserved during contraction, and that the core rotates as a solid body. For this analysis, we assume a fixed $r_\nu = 30$ km.

We find that, as expected, more rapidly rotating cases have lower critical curves, i.e., for a given mass accretion rate \dot{M} , the critical sound speed c_T is smaller for large Ω than for small Ω . For $\Omega/\Omega_{ms} = 1$, the critical curve only decreases by ~ 5 per-cent, indicating that, for these parameters and for this model problem, rotation has a relatively small effect on

¹ The equations are also solved by $\xi_{th} = 0$, but this solution is unphysical.

² In the full-physics case, the function instead gives the core neutrino luminosity L_ν (Burrows & Goshy 1993; Pejcha & Thompson 2012).

the critical curve. In terms of the critical antesonnic ratios, this rotational velocity corresponds to $\xi_{\text{cen}} = 7.08 \times 10^{-3}$ (for $r_{\text{sh}} = 150 \text{ km}$), which means the critical thermal antesonnic ratio is $\xi_{\text{th}} \simeq 0.1851$, a 1 per-cent decrease. When we instead assume solid-body rotation ($v_\phi(r) \propto r$) for the post-shock profile in solving Equation (13), we find larger fractional decreases in the critical curve for the same core rotation Ω because the rotational velocity at the shock will be larger.

We also note that each critical curve has a maximum mass accretion rate, which decreases with more rapid rotation. For larger accretion rates and more rapid rotation, the shock radius of the critical solution is smaller; for sufficiently large \dot{M} or Ω , the shock radius will be smaller than the PNS radius, which is unphysical. The ultimate physical limit on rotation is $\xi_{\text{cen}} = \frac{1}{2}$, as above this value, Equation (14) implies that $\xi_{\text{th}} < 0$, i.e., stable accretion is impossible at any sound speed. The limit of $r_{\text{sh}} > r_\nu$ provides a slightly more stringent limit, and other constraints, such as shock heating of the accreted material, or neutrino heating from the PNS core, will also tend to decrease the “maximum” rotation rate. We intend to further explore such constraints in future work.

While rotation rates $\Omega \sim \Omega_{\text{ms}}$ may be relevant for core collapses that produce super-luminous magnetar-powered supernovae or gamma-ray bursts (Thompson et al. 2004; Metzger et al. 2007; Kasen & Bildsten 2010; Metzger et al. 2011), they are much faster than expected for normal pulsars, which have $P \sim 10 - 1000 \text{ ms}$ (e.g., Faucher-Giguère & Kaspi 2006). Note that for clarity here we focus exclusively on the effect of the centrifugal force in the equatorial plane. In a more realistic model, especially at the rapid rotation rates needed for modification of the critical curve found here, other multi-dimensional effects become important (e.g., Yamasaki & Yamada 2005).

2.2 Turbulence

We now consider the problem of a non-rotating, but turbulent flow beneath the shock. We further assume that the flow is fully non-turbulent above the shock, i.e., that the turbulence is caused by neutrino heating and convection in the gain region (Herant et al. 1994; Janka & Müller 1996; Burrows et al. 1995) or the standing accretion shock instability (Blondin et al. 2003; Couch & O’Connor 2014; Fernández 2015), as obtained by multi-dimensional supernova simulations. For a turbulent flow, we must separate each fluid variable f into its background (i.e., Favre-averaged) component \bar{f} and its turbulent component f'' (Mocák et al. 2014):

$$f = \bar{f} + f''. \quad (17)$$

The Favre average is defined as:

$$\bar{\rho} \bar{f} = \overline{\rho f}, \quad \bar{f}'' = 0, \quad (18)$$

where \bar{f} is the Reynolds average

$$\bar{f} = \frac{1}{\Delta T} \int_T f(t) dt. \quad (19)$$

The Favre average is thus a density-weighted Reynolds average. While others (Meakin & Arnett 2007; Arnett et al. 2009; Murphy & Meakin 2011) use the Reynolds average, we prefer the Favre average for reasons of mathematical convenience. Starting with the full, time-steady Euler equations,

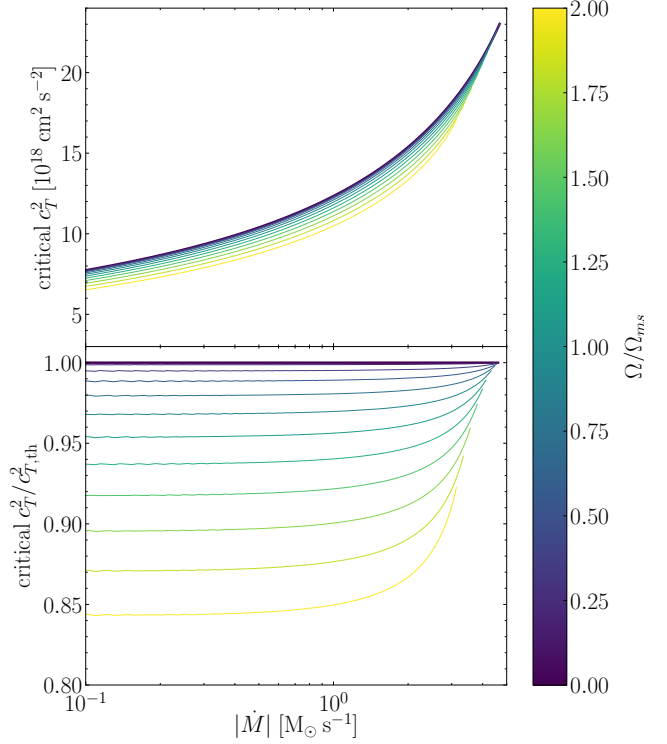


Figure 2. The critical sound speed c_T for a given accretion rate \dot{M} , for varying core rotation rates Ω , for the same PNS mass and radius as in Figure 1. Ω is shown in units of Ω_{ms} , the rotation rate that produces a millisecond rotator after contraction (i.e., accounting for angular momentum conservation). Faster rotation lowers the critical curve, i.e., reduces the critical c_T^2 for a given \dot{M} . Faster rotation also lowers the maximum accretion rate that shocked accretion can support (above which, $R_{\text{sh}} < R_\nu$). The bottom panel shows the ratio of the critical curves for different rotation rates to the non-rotating curve.

presented here in vector form:

$$\nabla \cdot (\rho \mathbf{v}) = 0 \quad (20)$$

$$\nabla \cdot (\rho \mathbf{v} \otimes \mathbf{v}) + \nabla P - \rho \mathbf{g} = 0 \quad (21)$$

We then decompose \mathbf{v} into its background and turbulent components, and take the Reynolds average of each equation. This leaves us with

$$\nabla \cdot (\bar{\rho} \tilde{\mathbf{v}}) = 0 \quad (22)$$

$$\bar{\rho} \tilde{\mathbf{v}} \cdot \nabla \tilde{\mathbf{v}} + \nabla \cdot \tilde{\mathbf{R}} + \nabla \bar{P} - \bar{\rho} \mathbf{g} = 0. \quad (23)$$

Here, $\tilde{\mathbf{R}}$ is the Reynolds stress tensor, which characterizes the strength of turbulence. Its components are given by

$$\tilde{R}_{ij} = \overline{\rho v_i'' v_j''}. \quad (24)$$

For our purposes, however, it is helpful to write things in terms of the specific turbulent kinetic energy:

$$K = \sum_i \frac{1}{2} \overline{v_i'' v_i''} = \frac{1}{2\bar{\rho}} \sum_i \tilde{R}_{ii}. \quad (25)$$

We can characterize the degree of isotropy in the turbulence by comparing the kinetic energy in turbulent radial velocity

to that in turbulent angular velocities:

$$\alpha \equiv \frac{\widetilde{R_{\theta\theta}} + \widetilde{R_{\phi\phi}}}{\widetilde{R_{rr}}}. \quad (26)$$

A value of $\alpha = 2$ corresponds to isotropic turbulence, while $\alpha = 1$ corresponds to anisotropic turbulence with $\widetilde{R_{rr}} = \widetilde{R_{\theta\theta}} + \widetilde{R_{\phi\phi}}$, which is a better fit to the character of turbulence in the gain region (Arnett et al. 2009; Murphy et al. 2013; Couch & Ott 2015; Radice et al. 2016). We can also make use of this parameter to define the total turbulent kinetic energy solely in terms of the radial Reynolds stress:

$$K = \frac{1 + \alpha}{2\bar{\rho}} \widetilde{R_{rr}} \quad (27)$$

Assuming an isothermal equation of state, spherical symmetry, and

$$\frac{\partial K}{\partial r} = 0, \quad (28)$$

(an assumption required for a tractable analytic solution), we can write the Euler equations in the dimensionless form:

$$(\widetilde{\mathcal{M}} - \widetilde{\mathcal{M}}^{-1}) \frac{\partial \widetilde{\mathcal{M}}}{\partial \xi_{\text{eff}}} - \frac{2}{\xi_{\text{eff}}} + \frac{\Xi_1}{2\xi_{\text{eff}}^2} = 0, \quad (29)$$

where

$$\widetilde{\mathcal{M}} = \frac{\widetilde{v_r}}{c_{\text{eff}}} \quad (30)$$

$$c_{\text{eff}}^2 = c_T^2 + \frac{2K}{1 + \alpha} \quad (31)$$

$$\xi_{\text{eff}} = \frac{c_{\text{eff}}^2}{v_{\text{esc}}^2} \quad (32)$$

$$\Xi_1 = 1 + 2 \frac{2 - \alpha}{1 + \alpha} \xi_{\text{turb}} \quad (33)$$

$$\xi_{\text{turb}} = \frac{2K}{v_{\text{esc}}^2}. \quad (34)$$

The full derivation of the Favre-averaged Euler equations is presented in Appendix B. We derive the antesonic condition under both isotropic and anisotropic turbulence in the following sub-sections.

We note that many studies describe the strength of turbulence in the post-shock region by the turbulent Mach number (e.g., Müller & Janka 2015), which is nominally related to our turbulent antesonic ratio by

$$\xi_{\text{turb}} \sim \xi_{\text{th}} \widetilde{\mathcal{M}_{\text{turb}}^2}, \quad (35)$$

where

$$\widetilde{\mathcal{M}_{\text{turb}}^2} = \frac{\widetilde{v_r'' v_r''}}{c_T^2} \quad (36)$$

However, care needs to be taken to account for the mix between radial and non-radial turbulent motions. We return to this issue in Section 3.

2.2.1 Isotropic Turbulence

For isotropic turbulence ($\alpha = 2$), the turbulent contribution to Ξ_1 vanishes. That is:

$$(\widetilde{\mathcal{M}} - \widetilde{\mathcal{M}}^{-1}) \frac{\partial \widetilde{\mathcal{M}}}{\partial \xi_{\text{eff}}} - \frac{2}{\xi_{\text{eff}}} + \frac{1}{2\xi_{\text{eff}}^2} = 0. \quad (37)$$

This is identical to the pure isothermal case (Equation 6) with the substitution $c_T \rightarrow c_{\text{eff}}$. A treatment of the shock-jump conditions similar to that of the pure isothermal case (see Appendix C for a full derivation) gives us an equation like Equation (8) with $c_T \rightarrow c_{\text{eff}}$:

$$\widetilde{\mathcal{M}}_1 = \frac{1}{2} \left(-\xi_{\text{eff}}^{-1/2} + \sqrt{\xi_{\text{eff}}^{-1} - 4} \right). \quad (38)$$

Since both our Euler equation and shock-jump condition are the same as in the pure isothermal case, except with $\xi_{\text{th}} \rightarrow \xi_{\text{eff}}$, the solution to this pair of equations – i.e., the antesonic condition – must be the same as the pure isothermal antesonic condition, except with $\xi_{\text{th}} \rightarrow \xi_{\text{eff}}$, i.e.,

$$\xi_{\text{eff}} = \xi_{\text{th}} + \frac{1}{3} \xi_{\text{turb}} = \frac{3}{16}. \quad (39)$$

We note that this antesonic condition has a critical threshold at $\xi_{\text{turb}} = \frac{9}{16}$, which corresponds to a turbulent kinetic energy of

$$K_{\text{max}} = \frac{9}{32} v_{\text{esc}}^2 \quad (40)$$

at the shock. Above this threshold, a steady accretion flow cannot be maintained at *any* finite value of the post-shock sound speed ($\xi_{\text{th}} > 0$). Like in the case with rotation, however, this limit is merely an upper bound on the maximum turbulent kinetic energy for which stable accretion is possible. Because the material is heated as it passes through the shock and then heated throughout the gain region, we expect the practical limit on K to be smaller. This will be the subject of a future investigation.

2.2.2 Anisotropic Turbulence

Anisotropic turbulence with $\alpha = 1$ is more characteristic of turbulence in the gain region than isotropic turbulence (Arnett et al. 2009; Murphy et al. 2013; Couch & Ott 2015; Radice et al. 2016). With this prescription, the Euler equation becomes:

$$(\widetilde{\mathcal{M}} - \widetilde{\mathcal{M}}^{-1}) \frac{\partial \widetilde{\mathcal{M}}}{\partial \xi_{\text{eff}}} - \frac{2}{\xi_{\text{eff}}} + \frac{1 + \xi_{\text{turb}}}{2\xi_{\text{eff}}^2} = 0. \quad (41)$$

This equation is analogous to the rotational case, but with $\xi_{\text{cen}} \rightarrow -\frac{1}{2} \xi_{\text{turb}}$ and $c_T \rightarrow c_{\text{eff}}$. As the shock-jump conditions imply the same functional form of the post-shock Mach number as in the isotropic case (i.e., Equation (38)), this implies that our antesonic condition must be

$$\xi_{\text{th}} + \frac{1}{2} \xi_{\text{turb}} = \frac{1}{32} \left(3 + 8\xi_{\text{turb}} + \sqrt{9 - 16\xi_{\text{turb}}} \right). \quad (42)$$

which can be directly compared to Equations (9) and (14) for the pure isothermal antesonic condition and the antesonic condition with rotation, respectively. We note that this equation has a root at $\xi_{\text{turb}} = 1/2$, which corresponds to a maximum value of the turbulent kinetic energy of

$$K_{\text{max}} = \frac{1}{4} v_{\text{esc}}^2 \quad (43)$$

at the shock – similar to, though slightly smaller than, the similar limit for isotropic turbulence given in Equation (40). As in the isotropic case, we expect the practical limit on K to be significantly less than this value because of shock heating and neutrino heating in the gain region, an issue we will return to in a future work.

In the limit where $\xi_{\text{turb}} \ll 1$, Equation (42) has the approximate form

$$\xi_{\text{th}} + \frac{1}{3}\xi_{\text{turb}} = \frac{3}{16}. \quad (44)$$

We use the same procedure used in constructing Figure 2 to calculate the critical curves for isotropic to anisotropic turbulence in Figure 3. For many different values of \dot{M} , we determine the critical value of the sound speed above which accretion is impossible, for a range of values of K . We see that with increasing turbulent kinetic energy (larger K/c_T^2), the normalization of the critical curve decreases. We also see that, except at the highest mass accretion rates, the decrease in normalization is roughly constant with \dot{M} . In Figure 4, we visually demonstrate the turbulent antesononic condition (Equation 42). The figure is analogous to Figure 1, except that we vary the ratio K/c_T^2 while keeping c_T constant. We find that, like with increasing c_T in the case dominated by thermal pressure, increasing the turbulent kinetic energy moves the shock radius outwards until the critical solution is reached.

Importantly, this exercise shows that for values of K/c_T^2 obtained in multi-dimensional supernova simulations (e.g., Murphy et al. 2013; Couch & Ott 2015; Radice et al. 2016; Mabanta & Murphy 2018), the fractional decrease in the critical curve at fixed \dot{M} can be large. While simulations find a range of turbulent kinetic energies as a function of both radius and time in a given massive star progenitor, values of K are often in the near-sonic range, with $K/c_T^2 \sim 1$, implying order-unity decrease to critical curve.

2.2.3 Power Law $K(r)$ Profiles

In our analysis, we assume that the turbulent kinetic energy density $K(r)$ is constant with radius (Equation 28), as this assumption allows us to find a straightforward analytic solution to the problem. However, simulations (Radice et al. 2016) suggest a power law $K(r) \propto r^\beta$ might be more appropriate. From that study in particular, we could approximate $K \propto r^3$ in the gain region. The general effect of such a parameterization would be to have stronger turbulence near the shock than near the core. Though we also note that turbulence enters the momentum equation as $\partial(\bar{\rho}K)/\partial r$ so that if K increases with r , then this will dampen the effect of the turbulent pressure gradient.

We tested numerical models with a power-law $K(r)$ and found that, compared to models with the same $K(r_\nu)$ but constant $K(r)$, power-law models with $\beta > 0$ had larger shock radii, and larger values of ξ_{turb} and ξ_{eff} at the shock. Furthermore, the critical solution had smaller $K(r_\nu)$, a smaller shock radius, and a larger ξ_{turb} and ξ_{eff} at the shock than the critical solution of the constant $K(r)$ model. For the $\beta < 0$ case, the reverse was true: for a given $K(r_\nu)$, the power law model had a smaller shock radius, and smaller ξ_{turb} and ξ_{eff} at the shock. The critical solution occurred at larger $K(r_\nu)$, and had a larger shock radius, and smaller ξ_{turb} and ξ_{eff} at the shock. However, although the critical solutions occur at different ξ_{th} and ξ_{turb} , we find that these values still respect the critical curve as defined in Equations (39) and (42).

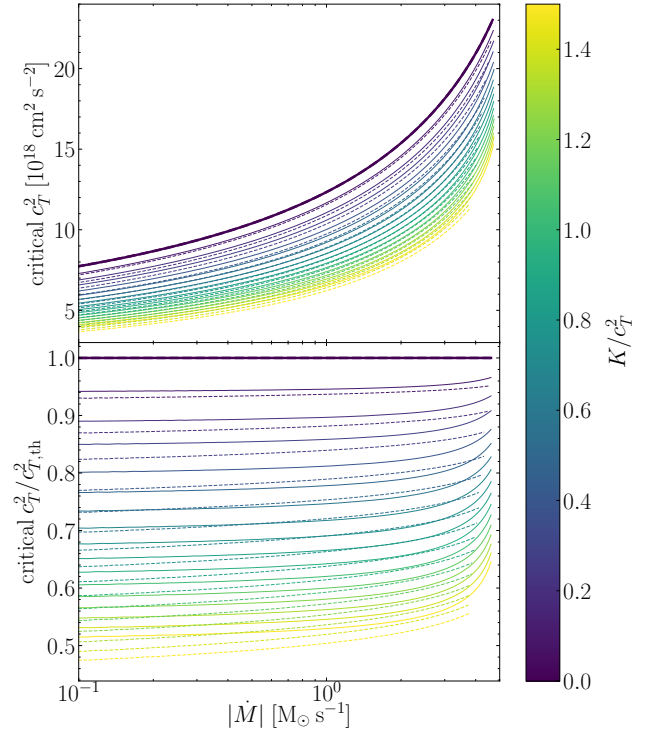


Figure 3. The critical curve for varying turbulent kinetic energies (shown here in units of c_T^2), for both isotropic (solid) and anisotropic (dashed) turbulence. We see that stronger turbulence lowers the critical curve, and that anisotropic turbulence also has a lower critical curve than isotropic turbulence does. Turbulence, both isotropic and anisotropic, has a larger effect on the critical curve at lower \dot{M} .

2.3 Combining Rotation and Turbulence

We can write the antesononic condition without specifying the exact nature of the turbulent balance (i.e., for arbitrary α), while also including rotation. This condition takes the form:

$$\xi_{\text{eff}} = \frac{1}{32} \left(8\Xi_2 + \sqrt{25 - 16\Xi_2} - 5 \right), \quad (45)$$

where (see Equations 11 and 33-34)

$$\Xi_2 = \Xi_1 - 2\xi_{\text{cen}}. \quad (46)$$

In the limits $\xi_{\text{cen}} \ll 1$, $\xi_{\text{turb}} \ll 1$, this reduces to

$$\xi_{\text{th}} + \frac{1}{3}\xi_{\text{cen}} + \frac{1}{3}\xi_{\text{turb}} = \frac{3}{16}. \quad (47)$$

3 DISCUSSION

3.1 An Antesononic “Ansatz”

Both rotation and turbulence add to the critical condition in a manner that is to first order quite straightforward and intuitive. A simple, but useful way to think about any additional forces that could be added to the Euler equation, is that they will add to the isothermal antesononic condition in

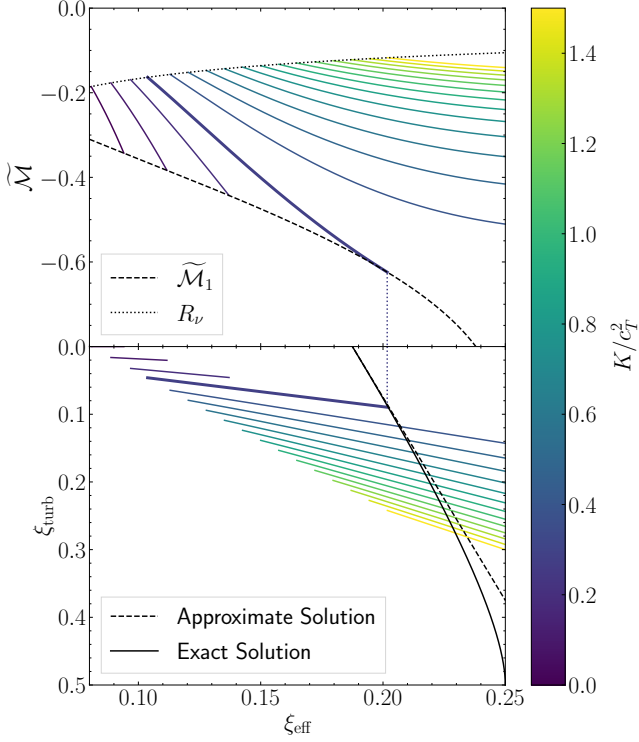


Figure 4. A visual demonstration of Equation (42), analogous to Figure 1. Top: the Mach number \tilde{M} vs the effective antesonic ratio $\xi_{\text{eff}} = c_{\text{eff}}^2 r / 2GM = \xi_{\text{th}} + \frac{1}{2}\xi_{\text{turb}}$, with curves color-coded by the ratio of K/c_T^2 (colors correspond to the same values of K/c_T^2 as in Figure 3). Though each of these curves has the same $c_T^2 = 10^{19} \text{ cm}^2 \text{ s}^{-2}$ and $\dot{M} = 1.0 M_{\odot}/\text{s}$, they start at different \tilde{M} and ξ_{eff} because of the K contribution to both those terms. Bottom: the turbulent antesonic ratio vs the effective antesonic ratio ξ_{turb} (note the reversed y-axis) for each solution shown in the top panel. The solid and dashed lines correspond to Equation (42) and Equation (44) (which is also the approximate critical curve for anisotropic turbulence), respectively. We see that the critical solution, which is bolded in each panel, just grazes the curve describing the Mach number at the shock (Equation 38) at the same point where it touches the curve describing the antesonic condition.

a similar manner:

$$\xi + \frac{1}{3}\xi_{\text{cen}} + \frac{1}{3}\xi_{\text{turb}} + \dots + a_i \xi_i \approx \frac{3}{16}, \quad (48)$$

where the ξ_i term takes the form

$$\xi_i = \frac{v_i^2}{v_{\text{esc}}^2}, \quad (49)$$

and a_i is a coefficient, with potentially negative values for terms that correspond to forces acting in the same direction as gravity. The v_i^2 here is the characteristic velocity (squared) for the force in question, where v_{ϕ}^2 and $2K$ are the relevant velocities for the cases of rotation and turbulence, respectively.

This “ansatz” for the form of a generalized antesonic condition allows for simple estimates of how big certain terms might in principle need to be in order to affect the dynamics. For example, if we were to consider a simple ra-

dial magnetic pressure term

$$P_{\text{mag}} = \frac{1}{2} \frac{B^2}{4\pi}, \quad (50)$$

(i.e., ignoring magnetic tension), the antesonic condition would contain the term

$$\xi_{\text{mag}} = \frac{v_A^2}{v_{\text{esc}}^2}, \quad a_{\text{mag}} = \frac{1}{2}, \quad (51)$$

in the simplest case where we assume $\partial v_A / \partial r = 0$. To significantly modify the critical curve, near-magnetosonic $v_A \sim c_T$ would be required, as might be expected from near-sonic turbulence (e.g., Ostriker et al. 2001). Recent studies (Müller & Varma 2020) suggest that magnetic fields can play a central role in explosion for $E_{\text{mag}} \sim \frac{1}{2} E_{\text{turb}}$. As with the case of turbulence considered above, other forms of $v_A(r)$ may lead to the same antesonic condition, but different shock radii for different normalizations of the post-shock magnetic field strength relative to the post-shock sound speed. As with rotation, there are many multi-dimensional effects that complicate the consideration of magnetic fields as an initiating agent in supernovae. Still, the simple ansatz of Equation (48) gives a starting point.

As another example that deserves more critical analysis, several works have considered the importance of wave driving, damping, and propagation in the post-shock region, generated by motions within the proto-neutron star (Burrows et al. 2006; Harada et al. 2017; Gossan et al. 2020). For a given wave flux into the gain region, the overall wave pressure gradient again enters the Euler equation for the post-shock flow in a manner similar to the turbulent pressure, except with

$$\widetilde{R}_{ij} \rightarrow 2\overline{P}_{ij}^{\text{aco}}, \quad (52)$$

where P^{aco} is the pressure from acoustic waves. For monochromatic, adiabatic sound waves, the ratio of angular to radial acoustic pressure is

$$\alpha = \frac{P_{\theta\theta} + P_{\phi\phi}}{P_{rr}} = 2 \frac{\gamma - 1}{\gamma + 1}, \quad (53)$$

where γ is the ratio of the specific heats (Lamers & Cassinelli 1999). Thus the acoustic pressure is strongly radially dominant, only approaching our case of anisotropic turbulence in the limit $\gamma \rightarrow \infty$. Ultimately, however, the acoustic term in the antesonic condition should look the same as the turbulent term, i.e.,

$$\xi_{\text{aco}} = \frac{2K_{\text{aco}}}{v_{\text{esc}}^2}, \quad a_{\text{aco}} = \frac{1}{3}. \quad (54)$$

Here K_{aco} is the specific acoustic kinetic energy:

$$K_{\text{aco}} = \frac{1}{2} \overline{v_{\text{aco}}^2} = \frac{1}{4} \omega^2 \zeta^2, \quad (55)$$

where v_{aco} is the velocity associated with acoustic motions, ω is the frequency of those oscillations, and ζ is the amplitude of the physical motion associated with the waves, i.e., a particle in the post-shock accretion flow traces a path governed by

$$r(t) = \bar{r}(t) + \zeta \cos(\omega t). \quad (56)$$

In recent calculations of acoustically powered explosions, Harada et al. (2017) found that successful explosions generally had lower thermal antesonic ratios (in their case,

$\max(c_s^2/v_{\text{esc}}^2)$ relative to failed explosions. In light of our work, this is expected because by increasing the acoustic power, [Harada et al. \(2017\)](#) are lowering the critical ξ_{th} below the maximum value of ξ_{th} reached in their non-exploding case. Specifically, [Harada et al. \(2017\)](#) use waves of frequency $\omega \sim 2 \text{ ms}^{-1}$ and amplitudes of order $\zeta \sim 5$ to 10 km near the shock. In our framework, this would result in an acoustic antesononic ratio of $\xi_{\text{aco}} \approx 0.03$ to 0.007 for a shock radius $r_{\text{sh}} = 150 \text{ km}$, and a 16 to 4 per-cent reduction in the critical thermal antesononic ratio ξ_{th} required for explosion. We note that the actual decrease in the critical neutrino luminosity found by [Harada et al. \(2017\)](#) is within this range.

3.2 1D Simulations with Turbulence

[Couch et al. \(2020\)](#) (hereafter in this section, CWO20) perform 1D supernova simulations using mixing length theory to approximate turbulence. The strength of turbulence is parameterized by α_{Λ} :

$$\alpha_{\Lambda} = \Lambda_{\text{mix}} \frac{\rho g}{P}, \quad (57)$$

where Λ_{mix} is the mixing length. The value $\alpha_{\Lambda} = 0$ corresponds to a simulation without turbulence, for which explosions are not achieved. As α_{Λ} increases above a certain threshold, progenitors begin to explode at different times, producing a range of explosion energies and neutron star masses. The results can be tuned to produce results for large surveys of progenitors and compared to the works of [Ugliano et al. \(2012\)](#); [Pejcha & Thompson \(2015\)](#); [Sukhbold et al. \(2016\)](#).

Because in CWO20 the strength of the turbulence is a free parameter, in principle, it should be possible to make an apposite comparison with our results. For small α_{Λ} and no explosion, the critical antesononic ratio should not be reached during the simulation, while models with bigger α_{Λ} just beyond the threshold for explosion should just exceed the critical generalized turbulent antesononic condition identified in Equation (42). That is, we expect a given model set with turbulence to explode only once the critical condition is exceeded.

In practice, the comparison is complicated by the fact that we have assumed an isothermal model for the gas, whereas the simulations use a general EOS and include neutrino heating/cooling. Nevertheless, we can attempt to make the comparison by first noting that a polytropic EOS ($P \propto \rho^{\Gamma}$) is a better fit to these models than the isothermal results presented in this paper. [Raives et al. \(2018\)](#) show analytically that the thermal antesononic ratio in the polytropic limit becomes (see also [Pejcha & Thompson 2012](#))

$$\frac{c_s^2}{v_{\text{esc}}^2} = \frac{3\Gamma}{16}. \quad (58)$$

Using this result and the calculations presented here (eq. 42), we can write down an approximate critical antesononic condition for a polytropic EOS with turbulence. While we are unable to derive a closed form analytic solution to the equations, we find an approximate numerical solution to the critical condition that is a good fit over the range of parameters we have tested:

$$\xi_{\text{total}} = \xi_{\text{th}} + \left(\frac{1}{3} + \frac{\Gamma - 1}{14.4205} \right) \xi_{\text{turb}} \approx \frac{3}{16} \Gamma. \quad (59)$$

Here, and throughout this section, ξ_{th} is the polytropic antesononic ratio given by Equation (58). Equation (59) is most accurate for small ξ_{turb} . Below $\xi_{\text{turb}} \sim 0.05$, the error in ξ_{total} from our approximate solution is $\lesssim 1$ per-cent for all $\Gamma \leq \frac{5}{3}$. As $\Gamma \rightarrow \frac{5}{3}$, (and as $\Gamma \rightarrow 1$, for which the approximation approaches Equation 44), a sub per-cent error in the critical condition is maintained for turbulent antesononic ratios as large as $\xi_{\text{turb}} \simeq 0.10 - 0.15$.

The work of [Pejcha & Thompson \(2012\)](#) shows that for models with neutrino heating/cooling and a general EOS that the antesononic condition is reached near the gain radius and that the antesononic condition is best represented in such cases by the maximum value achieved in the gain region, rather than just being evaluated at the shock as in the purely isothermal problem. Thus, for the purposes of comparison to CWO20, we take the total antesononic ratio to be

$$\xi_{\text{total}} = \max \left[\xi_{\text{th}} + \left(\frac{1}{3} + \frac{\Gamma - 1}{14.4205} \right) \xi_{\text{turb}} \right], \quad (60)$$

and we calculate this quantity throughout the time evolution of two progenitors, simulated with a range of α_{Λ} .

Understanding these caveats and with Equation 60 in hand, in Figure 5 we plot the total antesononic ratio as determined by the CWO20 simulations, for two different progenitor models: a $13 M_{\odot}$ and $15 M_{\odot}$ progenitor from the set used by [Sukhbold et al. \(2016\)](#). The location of the separatrix between accretion and wind (i.e., exploding) solutions occurs for $\xi \gtrsim 0.23$. For $\Gamma \simeq \frac{4}{3}$, as implied by the simulations at the maximum of ξ in the profiles, we would instead expect a critical value of $\xi \simeq 3\Gamma/16 = \frac{1}{4}$. Put another way, a value of $\Gamma \sim 1.23$ would be needed to make Equation 59 accord with the observed critical value in Figure 3. The ~ 10 per-cent difference between the expected critical value and that derived from the simulations is likely caused by differences between the physics of the simulations and the “pure” polytropic EOS analysis used to derive Equations (59) and (58). In particular, these simulations include an explicit coupling term between the turbulent and non-turbulent velocities that is not present in our analysis. Furthermore, these simulations include a general EOS and neutrino heating and cooling terms that are likewise absent from our models. Indeed, the accretion region between the proto-neutron star and the shock is not well-approximated by a single polytropic EOS. A focus of future work could be to make a more direct and sharper comparison of our results for the generalized antesononic condition with time-dependent numerical models by using more realistic thermodynamics.

3.3 Multidimensional Simulations

Since the pioneering work of [Herant et al. \(1994\)](#); [Burrows et al. \(1995\)](#); [Janka & Müller \(1995\)](#) evidence has accumulated that breaking spherical symmetry leads core-collapse supernova simulations closer to the condition for explosion. Indeed, many 1D models in the literature fail ([Rampp & Janka 2000](#); [Liebendörfer et al. 2001](#); [Thompson et al. 2003](#)), while their multi-dimensional counterparts sometimes succeed (but, see [O’Connor & Couch 2018](#)), albeit with low explosion energies in some cases (e.g., [Vartanyan et al. 2019](#)). The first study of the [Burrows & Goshy \(1993\)](#) critical curve in 2D by [Murphy & Burrows \(2008\)](#) showed that the critical threshold in neutrino luminosity for explosion was lower

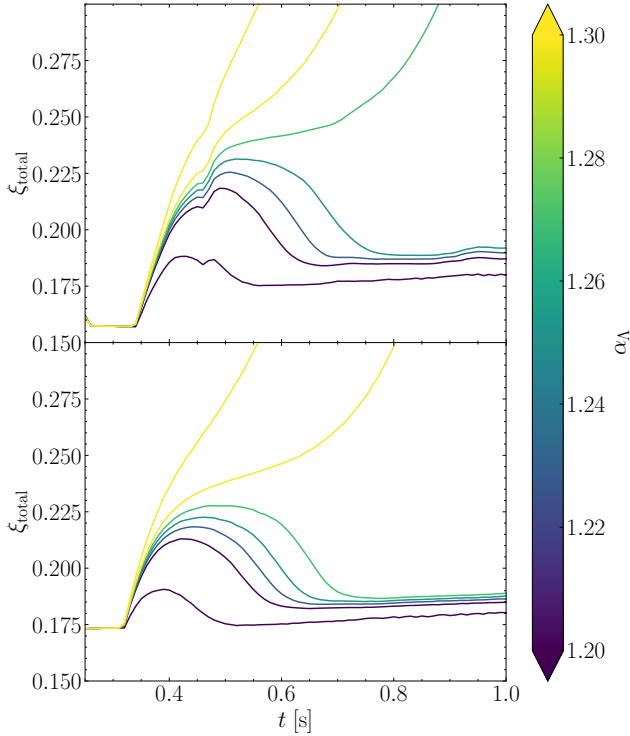


Figure 5. Total antesonic ratio (Equation 60) as a function of time for different values of the turbulent parameter α_A . The top panel uses a $13 M_\odot$ progenitor and the bottom panel uses a $15 M_\odot$ progenitor. We see that, by increasing α_A , we can induce explosion in otherwise stable configurations. Though the transition from accretion to wind solutions occurs at slightly lower ξ than we might expect, this can largely be attributed to differences between the simulation and the “pure” polytropic analysis.

than in 1D at a given mass accretion rate. That investigation was followed by a number of works on the critical threshold for explosion in multi-dimensional simulations (e.g., Nordhaus et al. 2010; Couch 2013b).

These works and many others show that the character and strength of the post-shock turbulence has a direct impact on the shock dynamics with time-dependent and progenitor-dependent thresholds for explosion. However, much of the discussion of the critical condition for explosion and the success or failure of any given model is qualitative in the sense that there has so far not been a quantitative theory for how much turbulence ‘helps’ in bringing models to explosion. There are a number important exceptions, including Müller & Janka (2015) (discussed below), the work of Couch et al. (2020) (discussed above), and Murphy et al. (2013); Couch & Ott (2015) who argue on the basis of momentum balance at the shock that turbulence leads to larger shock radii, and that this aids explosion (see also Couch & O’Connor 2014; Radice et al. 2016).

Here, our extension of the antesonic condition including rotation and turbulence in Equation (45), and the generalized “ansatz” for other forces in Equation (48) provides a simple and intuitive quantitative criterion for explosion, albeit for a toy model. Specifically, the threshold for explosion in multi-dimensional simulations is lower because the crit-

ical threshold for the thermal energy content of matter in the post-shock region is lower by (Equation 42)

$$\xi_{\text{th}} \simeq \frac{3}{16} - \frac{1}{3}\xi_{\text{turb}} \quad (61)$$

(for small ξ_{turb}). The physics of this condition is the same as for the antesonic condition itself: above a certain critical value of the linear combination of ξ_{th} and ξ_{turb} it is impossible to simultaneously satisfy the strong shock jump conditions and the time-steady Euler equation and the system undergoes time-dependent transition from accretion to thermal wind. Because the strength and character (i.e., level of isotropy) of the turbulence varies as a function of progenitor and time, the exact values of ξ_{th} and ξ_{turb} will likewise also vary with progenitor and time.

While much work remains in attempting to apply this condition to multi-dimensional, full physics models, this explosion condition is useful as a prior on which models will explode and which will fail, and potentially provides the physical explanation for the explosion itself. Future works can directly test if an equation like (42) is indeed the correct way to think about this threshold.

In this context, ideally we would be able to make a direct connection between the explosion condition of Equation (42) and the results of multi-dimensional simulations. One example is the work of Müller & Janka (2015) (hereafter in this section, MJ15) who perform 2D simulations with turbulence, and find a threshold in the turbulent Mach number above which all of their simulations explode. However, the comparison with MJ15 is complicated by several factors. MJ15 define the turbulent Mach number using the angular turbulent velocity rather than the radial, i.e.,

$$\widetilde{\mathcal{M}}_{\text{MJ15}}^2 = \frac{v_\theta'' v_\theta''}{c_s^2}. \quad (62)$$

This differs from our definition of the turbulent Mach number by a factor of $1/\alpha$:

$$\widetilde{\mathcal{M}}_{\text{turb}}^2 \sim \frac{1}{\alpha} \widetilde{\mathcal{M}}_{\text{MJ15}}^2. \quad (63)$$

To obtain the specific turbulent kinetic energy K , which enters our definition of ξ_{turb} we must further multiply by a factor of $1 + \alpha$ to account for both the radial and non-radial motions:

$$\frac{1}{2} \frac{\xi_{\text{turb}}}{\xi_{\text{th}}} = \frac{K}{c_T^2} = \frac{1 + \alpha}{2} \widetilde{\mathcal{M}}_{\text{turb}}^2 = \frac{1 + \alpha}{2\alpha} \widetilde{\mathcal{M}}_{\text{MJ15}}^2. \quad (64)$$

An additional complication is that to make a direct comparison between MJ15 and this work requires knowledge of the relative strength of radial and non-radial turbulent motions (quantified by α) at the time of explosion, which MJ15 do not provide. While MJ15 initialize their simulations with a wide range of α (up to $\alpha \simeq 17$), we assume α evolves to equipartition between the radial and non-radial motions (i.e., $\alpha = 1$; Arnett et al. 2009) by the time of explosion.

Furthermore, while here we have explored a wide, two-dimensional parameter space of ξ_{th} and ξ_{turb} , for many different steady-state values of the mass accretion rate (e.g., Fig. 4) in MJ15 the post-shock sound speed (and thus, ξ_{th}) set by neutrino heating and cooling, the accretion rate, and the shock radius, which is determined by *both* the sound speed and the specific turbulent kinetic energy K . Thus,

the critical condition found by MJ15 is essentially for fixed ξ_{th} . While we cannot determine what ξ_{th} was at explosion in the simulations of MJ15, we can determine what the critical ξ_{th} would be in our model using the critical turbulent Mach number found by MJ15.

MJ15 finds a critical turbulent Mach number

$$\widetilde{\mathcal{M}}_{\text{MJ15}}^2 \simeq 0.3. \quad (65)$$

For $\alpha = 1$, this corresponds to the same value of $\widetilde{\mathcal{M}}_{\text{turb}}^2$. Using the approximate antesononic condition for the polytropic equation of state we found earlier (Equation 59), we would expect the critical thermal antesononic ratio to be

$$\xi \approx 0.227 \quad (66)$$

for $\Gamma = \frac{4}{3}$. This is about a 10 per-cent decrease from the limit of $\frac{3}{16}\Gamma = \frac{1}{4}$. Put another way, if we assume a one-to-one correspondence between the critical neutrino luminosity and the critical c_s^2 (i.e., a factor of 2 change in one means a factor of 2 change in the other), then the 25 per-cent change in the critical neutrino luminosity measured by MJ15 would mean a critical total antesononic ratio of

$$\xi_{\text{total}} \approx 0.21, \quad (67)$$

assuming the same critical turbulent Mach number. This is about 15 per-cent below what our analytic theory predicts, similar to the discrepancy we found between our theory and the results of Couch et al. (2020) in the previous section. Likewise, we can attribute this discrepancy to the difference between our simplified use of a “pure” polytropic EOS and the physical EOS used by MJ15. There is also the potential for the dynamical effects of turbulence, in particular, oscillations in the shock surface, to lower the critical curve, as in the work of Murphy & Burrows (2008) and Gabay et al. (2015).

4 CONCLUSIONS

We demonstrate that both rotation and turbulence reduce the critical antesononic ratio in our 1D, isothermal model. We emphasize that attempting to characterize a simulation only by the thermal antesononic ratio can be misleading. In a model with significant rotation or turbulence, we would expect the critical value of ξ to be measurably smaller than one would expect from the non-turbulent analysis.

Specifically, if we consider our first order approximation to the antesononic condition (Equation 47), this is equivalent to stating that

$$\xi_{\text{th,crit}} = \frac{3}{16} - \frac{1}{3}\xi_{\text{cen}} - \frac{1}{3}\xi_{\text{turb}}. \quad (68)$$

As discussed in §3.3, in this picture, multi-dimensional models are easier to explode than their spherical counterparts because the turbulent pressure in the post-shock region and at the shock decreases the critical sound speed required for explosion. In a comparison like that presented in Nagakura et al. (2019), where a low-resolution model fails and a high-resolution model succeeds, we would interpret the success and failure in terms of the critical condition above (see also Raives et al. 2018, where we discuss the effect of resolution on the critical condition). As discussed in §2.2 (see Figure 4) and §3.2, the turbulent Mach numbers needed to substantially affect the critical condition are typical of the results of

multi-dimensional simulations. For example, Couch & Ott (2015) finds ratios of turbulent to thermal pressure of up to $K/c_T^2 \sim 0.5$; in our model that would correspond to a decrease of the critical curve normalization (i.e., the critical c_T^2 for a given \dot{M}) of 15 to 25 per cent (decreasing with larger \dot{M}). For rotation, the effect is less significant, with a rotation rate corresponding to a millisecond period remnant only leading to a 1 to 4 per cent decrease. Faster rotation rates can lead to more modest decreases in the critical curve normalization, but we quickly reach rotation rates that would lead to remnants rotating much faster than supported by observation, and rates approaching the limits discussed in §2.1.

We also explore the potential of an antesononic “ansatz” to describe the effects of other forces on the critical condition for explosion. Our analysis suggests that there is an antesononic ratio (i.e., some characteristic velocity squared divided by the escape velocity squared) associated with each force, and that, to first order, the critical condition can be expressed as a linear combination of these terms. As examples, we briefly discuss magnetic pressure and acoustic wave pressure in the context of this framework.

In our models, we find theoretical maximum values of $\xi_{\text{cen}} = \frac{1}{2}$ and $\xi_{\text{turb}} = \frac{1}{2}, \frac{9}{16}$ (for isotropic and anisotropic turbulence, respectively). Our antesononic “ansatz” suggests similar limits exist for other forces. At these values of the non-thermal antesononic ratio, the pressure behind the shock is large enough to lead to explosion even in the absence of thermal pressure. However, in nature, we cannot actually reach this hypothetical limit of zero thermal pressure. Even in the absence of neutrino heating from the PNS core, the accreting material will be shock heated as it passes the shock, providing a minimum thermal pressure and thus minimum thermal antesononic ratio. Because of this, the actual maximum non-thermal antesononic ratios will be smaller than the limits presented in this paper. In future work, we will self-consistently consider the effect of shock heating and the limits it imposes on non-thermal contributions to explosion.

However, we stress that an exploration of these effects in full-physics supernova simulations is required before we can make specific numerical predictions about those cases. In non-isothermal simulations of this problem, the numerical value of the antesononic condition will generally change. As shown by Raives et al. (2018), in the case that the post-shock fluid is described by an EOS of the form $P \propto \rho^\Gamma$, the antesononic condition is $c_s^2/v_{\text{esc}}^2 = 3\Gamma/16$ at the shock, where $c_s = (\Gamma P/\rho)^{1/2}$ is the adiabatic sound speed. Similarly, for an equation of state coupled to neutrino heating and cooling, Pejcha & Thompson (2012) showed that an antesononic condition of $\xi_{\text{crit}}^\nu \equiv \max(c_s^2/v_{\text{esc}}^2) \sim 0.2$ was a good fit over several orders of magnitude, though later multidimensional simulations have suggested a wider range of critical antesononic ratios, $\xi_{\text{crit}}^\nu \sim 0.2 - 0.3$ (Couch & Ott 2013; Dolence et al. 2013; Couch & O’Connor 2014).

We also note that our results on rotation suggest that rapidly rotating stars should be easier to explode near the equator (where v_ϕ is the largest), in contrast to Yamasaki & Yamada (2005) which prefers polar explosions. In reality, these are not two contradictory results but two competing effects. We find that the critical thermal antesononic ratio is smallest at the equator (implying explosion should initiate there), while Yamasaki & Yamada (2005) find that rotation

focuses the accreting material towards the equator, decreasing the accretion rate at the poles (implying explosion should commence along the rotation axis). Which of these two effects win out will likely depend on details of the equation of state, as well as the relative values of v_ϕ , P_{th} , and $\dot{M}(t)$. E.g., we might naïvely expect models with extreme accretion rates to care more about the distribution of accretion over the shock surface, while models with very small accretion rates and/or small thermal pressures might care more about the reduction in ξ_{crit} near the equator. Regardless, such questions must be answered with 2D and 3D simulations of this problem and must wait, ideally, for a multi-D theory of the antesonic condition to be developed.

ACKNOWLEDGEMENTS

MJR and TAT thank Davide Radice, Bernhard Müller, and Ondrej Pejcha for helpful conversations. TAT acknowledges support from a Simons Foundation Fellowship and an IBM Einstein Fellowship from the Institute for Advanced Study, Princeton. TAT and MJR also acknowledge partial support from NASA grant 80NSSC20K0531.

SMC is supported by the U.S. Department of Energy, Office of Science, Office of Nuclear Physics, Early Career Research Program under Award Number DE-SC0015904. This material is based upon work supported by the U.S. Department of Energy, Office of Science, Office of Advanced Scientific Computing Research and Office of Nuclear Physics, Scientific Discovery through Advanced Computing (SciDAC) program under Award Number DE-SC0017955. This research was supported by the Exascale Computing Project (17-SC-20-SC), a collaborative effort of the U.S. Department of Energy Office of Science and the National Nuclear Security Administration.

The research presented in this paper made use of the python libraries MATPLOTLIB (Hunter 2007), NUMPY (van der Walt et al. 2011), and SCIPY (Virtanen et al. 2020). It also makes use of YT-PROJECT (Turk et al. 2011).

DATA AVAILABILITY

The data underlying this article will be shared on reasonable request to the corresponding author. Requests for data originating from Couch et al. (2020) should be sent directly to SMC.

REFERENCES

- Arnett D., Meakin C., Young P. A., 2009, *ApJ*, 690, 1715
 Blondin J. M., Mezzacappa A., DeMarino C., 2003, *ApJ*, 584, 971
 Burrows A., Goshy J., 1993, *ApJ*, 416, L75
 Burrows A., Hayes J., Fryxell B. A., 1995, *ApJ*, 450, 830
 Burrows A., Livne E., Dessart L., Ott C. D., Murphy J., 2006, *ApJ*, 640, 878
 Couch S. M., 2013a, *ApJ*, 765, 29
 Couch S. M., 2013b, *ApJ*, 775, 35
 Couch S. M., O'Connor E. P., 2014, *ApJ*, 785, 123
 Couch S. M., Ott C. D., 2013, *ApJ*, 778, L7
 Couch S. M., Ott C. D., 2015, *ApJ*, 799, 5
 Couch S. M., Warren M. L., O'Connor E. P., 2020, *ApJ*, 890, 127
 Dolence J. C., Burrows A., Murphy J. W., Nordhaus J., 2013, *ApJ*, 765, 110
 Ertl T., Janka H.-T., Woosley S. E., Sukhbold T., Ugliano M., 2016, *ApJ*, 818, 124
 Faucher-Giguère C.-A., Kaspi V. M., 2006, *ApJ*, 643, 332
 Fernández R., 2015, *MNRAS*, 452, 2071
 Gabay D., Balberg S., Keshet U., 2015, *ApJ*, 815, 37
 Gossan S. E., Fuller J., Roberts L. F., 2020, *MNRAS*, 491, 5376
 Harada A., Nagakura H., Iwakami W., Yamada S., 2017, *ApJ*, 839, 28
 Herant M., Benz W., Hix W. R., Fryer C. L., Colgate S. A., 1994, *ApJ*, 435, 339
 Hunter J. D., 2007, *Computing In Science & Engineering*, 9, 90
 Iwakami W., Nagakura H., Yamada S., 2014, *ApJ*, 793, 5
 Janka H.-T., Müller E., 1995, *ApJ*, 448, L109
 Janka H. T., Müller E., 1996, *A&A*, 306, 167
 Kasen D., Bildsten L., 2010, *ApJ*, 717, 245
 Lamers H. J. G. L. M., Cassinelli J. P., 1999, *Introduction to Stellar Winds*. Cambridge University Press, <https://ui.adsabs.harvard.edu/abs/1999isw...book.....L>
 Liebendorfer M., Mezzacappa A., Thielemann F.-K., Messer O. E., Hix W. R., Bruenn S. W., 2001, *Phys. Rev. D*, 63, 103004
 Mabanta Q. A., Murphy J. W., 2018, *ApJ*, 856, 22
 Meakin C. A., Arnett D., 2007, *ApJ*, 667, 448
 Metzger B. D., Thompson T. A., Quataert E., 2007, *ApJ*, 659, 561
 Metzger B. D., Giannios D., Thompson T. A., Bucciantini N., Quataert E., 2011, *MNRAS*, 413, 2031
 Mocák M., Meakin C., Viallet M., Arnett D., 2014, arXiv e-prints
 Müller B., Janka H.-T., 2015, *MNRAS*, 448, 2141
 Müller B., Varma V., 2020, *MNRAS*
 Murphy J. W., Burrows A., 2008, *ApJ*, 688, 1159
 Murphy J. W., Dolence J. C., 2017, *ApJ*, 834, 183
 Murphy J. W., Meakin C., 2011, *ApJ*, 742, 74
 Murphy J. W., Dolence J. C., Burrows A., 2013, *ApJ*, 771, 52
 Nagakura H., Burrows A., Radice D., Vartanyan D., 2019, *MNRAS*, 490, 4622
 Nordhaus J., Burrows A., Almgren A., Bell J., 2010, *ApJ*, 720, 694
 O'Connor E. P., Couch S. M., 2018, *ApJ*, 854, 63
 O'Connor E., Ott C. D., 2011, *ApJ*, 730, 70
 Ostriker E. C., Stone J. M., Gammie C. F., 2001, *ApJ*, 546, 980
 Pejcha O., Thompson T. A., 2012, *ApJ*, 746, 106
 Pejcha O., Thompson T. A., 2015, *ApJ*, 801, 90
 Radice D., Ott C. D., Abdikamalov E., Couch S. M., Haas R., Schnetter E., 2016, *ApJ*, 820, 76
 Raives M. J., Couch S. M., Greco J. P., Pejcha O., Thompson T. A., 2018, *MNRAS*, 481, 3293
 Rampp M., Janka H. T., 2000, *ApJ*, 539, L33
 Sukhbold T., Ertl T., Woosley S. E., Brown J. M., Janka H.-T., 2016, *ApJ*, 821, 38
 Takiwaki T., Kotake K., Suwa Y., 2014, *ApJ*, 786, 83
 Thompson T. A., Burrows A., Pinto P. A., 2003, *ApJ*, 592, 434

Thompson T. A., Chang P., Quataert E., 2004, *ApJ*, 611, 380
 Turk M. J., Smith B. D., Oishi J. S., Skory S., Skillman S. W.,
 Abel T., Norman M. L., 2011, *ApJS*, 192, 9
 Ugliano M., Janka H.-T., Marek A., Arcones A., 2012, *ApJ*, 757,
 69
 Vartanyan D., Burrows A., Radice D., Skinner M. A., Dolence J.,
 2019, *MNRAS*, 482, 351
 Virtanen P., et al., 2020, *Nature Methods*, 17, 261
 Yamasaki T., Yamada S., 2005, *ApJ*, 623, 1000
 Yamasaki T., Yamada S., 2007, *ApJ*, 656, 1019
 van der Walt S., Colbert S. C., Varoquaux G., 2011, *Computing
 in Science Engineering*, 13, 22

APPENDIX A: PROPERTIES OF THE FAVRE AVERAGE

In this section, we review the definition and useful rules of the Favre average. Recall, for a field f , split into a (Favre-averaged) background and turbulent component

$$f = \tilde{f} + f'', \quad (\text{A1})$$

the Favre average is defined as:

$$\bar{\rho} \tilde{f} = \overline{\rho f}, \quad (\text{A2})$$

where \bar{f} is the Reynolds average

$$\bar{f} = \frac{1}{\Delta T} \int_T f(t) dt. \quad (\text{A3})$$

Note that by definition:

$$\tilde{f}'' = 0. \quad (\text{A4})$$

The Favre average is thus a density-weighted Reynolds average. Ultimately, the Favre average is an integration operator, and thus the normal rules for integration imply the following identities, which we make use of in the next section:

$$\overline{\rho(\tilde{f} + g)} = \bar{\rho}(\tilde{f} + \tilde{g}) \quad (\text{A5})$$

$$\bar{\rho}(\tilde{g} \cdot \tilde{f}'') = 0 \quad (\text{A6})$$

$$\bar{\rho} \tilde{f} = \overline{\rho f} \quad (\text{A7})$$

$$\overline{\rho(\tilde{f} \cdot g)} = \bar{\rho}(\tilde{f} \cdot \tilde{g}) \quad (\text{A8})$$

$$\frac{\partial \tilde{f}}{\partial s} = \frac{\partial \overline{f}}{\partial s}. \quad (\text{A9})$$

APPENDIX B: FAVRE-AVERAGED EULER EQUATIONS

We start with the full, time-steady Euler equations, presented here in vector form:

$$\nabla \cdot (\rho \mathbf{v}) = 0 \quad (\text{B1})$$

$$\nabla \cdot (\rho \mathbf{v} \otimes \mathbf{v}) + \nabla P - \rho \mathbf{g} = 0 \quad (\text{B2})$$

We then take decompose \mathbf{v} into its background component $\tilde{\mathbf{v}}$ and its turbulent component \mathbf{v}'' :

$$\nabla \cdot (\rho(\tilde{\mathbf{v}} + \mathbf{v}'')) = 0 \quad (\text{B3})$$

$$\nabla \cdot (\rho(\tilde{\mathbf{v}} + \mathbf{v}'') \otimes (\tilde{\mathbf{v}} + \mathbf{v}'')) + \nabla P - \rho \mathbf{g} = 0 \quad (\text{B4})$$

Then we take a Reynolds average of the full equation:

$$\overline{\nabla \cdot (\rho(\tilde{\mathbf{v}} + \mathbf{v}''))} = 0 \quad (\text{B5})$$

$$\overline{\nabla \cdot (\rho(\tilde{\mathbf{v}} + \mathbf{v}'') \otimes (\tilde{\mathbf{v}} + \mathbf{v}''))} + \nabla \bar{P} - \bar{\rho} \mathbf{g} = 0 \quad (\text{B6})$$

Using the rules outlined in the previous section:

$$\begin{aligned} \nabla \cdot (\rho(\tilde{\mathbf{v}} + \mathbf{v}'')) &= 0 \\ \nabla \cdot (\rho \tilde{\mathbf{v}} \otimes \tilde{\mathbf{v}} + \rho \mathbf{v}'' \otimes \mathbf{v}'') &= 0 \\ \nabla \cdot (\bar{\rho} \tilde{\mathbf{v}}) &= 0 \end{aligned} \quad (\text{B7})$$

And for the momentum equation:

$$\begin{aligned} \nabla \cdot (\rho(\tilde{\mathbf{v}} + \mathbf{v}'') \otimes (\tilde{\mathbf{v}} + \mathbf{v}'')) + \nabla \bar{P} - \bar{\rho} \mathbf{g} &= 0 \\ \nabla \cdot (\rho \tilde{\mathbf{v}} \otimes \tilde{\mathbf{v}} + 2\rho \tilde{\mathbf{v}} \otimes \mathbf{v}'' + \rho \mathbf{v}'' \otimes \mathbf{v}'') + \nabla \bar{P} - \bar{\rho} \mathbf{g} &= 0 \\ \nabla \cdot (\bar{\rho} \tilde{\mathbf{v}} \otimes \tilde{\mathbf{v}}) + \nabla \cdot \tilde{\mathbf{R}} + \nabla \bar{P} - \bar{\rho} \mathbf{g} &= 0. \end{aligned}$$

The divergence term we will transform as

$$\nabla \cdot (\bar{\rho} \tilde{\mathbf{v}} \otimes \tilde{\mathbf{v}}) = \tilde{\mathbf{v}}(\nabla \cdot (\bar{\rho} \tilde{\mathbf{v}})) + \bar{\rho} \tilde{\mathbf{v}} \cdot \nabla \tilde{\mathbf{v}}, \quad (\text{B8})$$

and thus we have

$$\bar{\rho} \tilde{\mathbf{v}} \cdot \nabla \tilde{\mathbf{v}} + \nabla \cdot \tilde{\mathbf{R}} + \nabla \bar{P} - \bar{\rho} \mathbf{g} = 0. \quad (\text{B9})$$

Here $\tilde{\mathbf{R}}$ is the Reynolds tensor, the components of which are:

$$\widetilde{R_{ij}} = \overline{\rho v_i'' v_j''} \quad (\text{B10})$$

Expressing Equations (B7) and (B9) in spherical coordinates, we obtain

$$\frac{1}{\bar{\rho}} \frac{\partial \bar{\rho}}{\partial r} + \frac{1}{\tilde{v}_r} \frac{\partial \tilde{v}_r}{\partial r} + \frac{2}{r} = 0 \quad (\text{B11})$$

$$\begin{aligned} \bar{\rho} \tilde{v}_r \frac{\partial \tilde{v}_r}{\partial r} - \bar{\rho} \frac{\tilde{v}_\phi \tilde{v}_\phi}{r} + \frac{\partial (\bar{P} + \widetilde{R_{rr}})}{\partial r} \\ + (2 - \alpha) \frac{\widetilde{R_{rr}}}{r} + \bar{\rho} \frac{GM}{r^2} = 0, \end{aligned} \quad (\text{B12})$$

where α is the degree of isotropy of the turbulence, as defined in Equation (26).

We can also write this equation in terms of the turbulent kinetic energy

$$K = \frac{1}{2} \sum_i \widetilde{v_i'' v_i''}. \quad (\text{B13})$$

Assuming $\frac{\partial K}{\partial r} = 0$ and an isothermal equation of state, we have

$$\begin{aligned} \tilde{v}_r \frac{\partial \tilde{v}_r}{\partial r} - \frac{\tilde{v}_\phi \tilde{v}_\phi}{r} + \frac{1}{\bar{\rho}} \left(c_T^2 + \frac{2K}{1 + \alpha} \right) \frac{\partial \bar{\rho}}{\partial r} \\ + \frac{2 - \alpha}{1 + \alpha} \frac{2K}{r} + \frac{GM}{r^2} = 0. \end{aligned} \quad (\text{B14})$$

Let $c_{\text{eff}}^2 = c_T^2 + \frac{2K}{1 + \alpha}$. Then:

$$\tilde{v}_r \frac{\partial \tilde{v}_r}{\partial r} - \frac{\tilde{v}_\phi \tilde{v}_\phi}{r} + \frac{c_{\text{eff}}^2}{\bar{\rho}} \frac{\partial \bar{\rho}}{\partial r} + \frac{2 - \alpha}{1 + \alpha} \frac{2K}{r} + \frac{GM}{r^2} = 0. \quad (\text{B15})$$

Substituting in Equation (B7),

$$\left(\tilde{v}_r - \frac{c_{\text{eff}}^2}{\tilde{v}_r} \right) \frac{\partial \tilde{v}_r}{\partial r} - \frac{\tilde{v}_\phi \tilde{v}_\phi}{r} - \frac{2c_{\text{eff}}^2}{r} + \frac{2 - \alpha}{1 + \alpha} \frac{2K}{r} + \frac{GM}{r^2} = 0. \quad (\text{B16})$$

Let $\xi_{\text{cen}} = \widetilde{v_\phi v_\phi} / v_{\text{esc}}^2$ and $\xi_{\text{turb}} = 2K / v_{\text{esc}}^2$. Then:

$$\frac{\widetilde{v_\phi v_\phi}}{r} = \frac{v_{\text{esc}}^2}{r} \frac{\widetilde{v_\phi v_\phi}}{v_{\text{esc}}^2} = \frac{2GM}{r^2} \xi_{\text{cen}} \quad (\text{B17})$$

$$\frac{2 - \alpha}{1 + \alpha} \frac{2K}{r} = \frac{2 - \alpha}{1 + \alpha} \frac{v_{\text{esc}}^2}{r} \frac{2K}{v_{\text{esc}}^2} = \frac{2 - \alpha}{1 + \alpha} \frac{2GM}{r^2} \xi_{\text{turb}}, \quad (\text{B18})$$

and we have:

$$\left(\widetilde{v_r} - \frac{c_{\text{eff}}^2}{\widetilde{v_r}} \right) \frac{\partial \widetilde{v_r}}{\partial r} - \frac{2c_{\text{eff}}^2}{r} + \frac{GM}{r^2} \Xi_2 = 0 \quad (\text{B19})$$

$$\Xi_2 = 1 - 2\xi_{\text{cen}} + 2\frac{2 - \alpha}{1 + \alpha} \xi_{\text{turb}} \quad (\text{B20})$$

Multiplying all terms by $2GM/c_{\text{eff}}^4$, and allowing $\widetilde{\mathcal{M}} = \widetilde{v_r}/c_{\text{eff}}$:

$$\left(\widetilde{\mathcal{M}} - \widetilde{\mathcal{M}}^{-1} \right) \frac{\partial \widetilde{\mathcal{M}}}{\partial \xi_{\text{eff}}} - \frac{2}{\xi_{\text{eff}}} + \frac{\Xi_2}{2\xi_{\text{eff}}^2} = 0, \quad (\text{B21})$$

where

$$\xi_{\text{eff}} = \frac{c_{\text{eff}}^2}{v_{\text{esc}}^2} \quad (\text{B22})$$

APPENDIX C: FAVRE-AVERAGED SHOCK-JUMP CONDITIONS

We start with the continuity and momentum shock-jump conditions:

$$\rho_1 v_1 = \rho_2 v_2 \quad (\text{C1})$$

$$\rho_1 v_1^2 + P_1 = \rho_2 v_2^2 + P_2, \quad (\text{C2})$$

Where $v = v_r$ is the radial velocity. As before, we take the Reynolds average of both equations:

$$\begin{aligned} \overline{\rho_1 v_1} &= \overline{\rho_2 v_2} \\ \overline{\rho_1 \widetilde{v_1}} &= \overline{\rho_2 \widetilde{v_2}} \end{aligned} \quad (\text{C3})$$

$$\begin{aligned} \overline{\rho_1 v_1^2 + P_1} &= \overline{\rho_2 v_2^2 + P_2} \\ \overline{\rho_1 \widetilde{v_1} \widetilde{v_1} + \rho_1 \widetilde{v_1}' \widetilde{v_1}'' + P_1} &= \overline{\rho_2 \widetilde{v_2} \widetilde{v_2} + \rho_2 \widetilde{v_2}' \widetilde{v_2}'' + P_2} \\ \overline{\rho_1 \widetilde{v_1} \widetilde{v_1} + \widetilde{R_1} + P_1} &= \overline{\rho_2 \widetilde{v_2} \widetilde{v_2} + \widetilde{R_2} + P_2}, \end{aligned} \quad (\text{C4})$$

where $R = R_{rr}$ is the radial Reynolds stress. Assuming there is no turbulence above the shock, these reduce to

$$\overline{\rho_1} \widetilde{v_1} = \rho_2 v_2 \quad (\text{C5})$$

$$\overline{\rho_1} \widetilde{v_1} \widetilde{v_1} + \widetilde{R_1} + \overline{P_1} = \rho_2 v_2^2 + P_2. \quad (\text{C6})$$

Assuming an isothermal EOS and pressureless free-fall above the shock:

$$\overline{\rho_1} \widetilde{v_1} = -\rho_2 \sqrt{\frac{2GM}{r}} \quad (\text{C7})$$

$$\begin{aligned} \overline{\rho_1} \widetilde{v_1} \widetilde{v_1} + \overline{\rho_1} \left(c_T^2 + \frac{2K}{1 + \alpha} \right) &= \rho_2 \frac{2GM}{r} \\ \overline{\rho_1} \widetilde{v_1} \widetilde{v_1} + \overline{\rho_1} c_{\text{eff}}^2 &= \rho_2 \frac{2GM}{r}. \end{aligned} \quad (\text{C8})$$

From here the solution proceeds analogously to the fully non-turbulent case; i.e.,

$$\widetilde{\mathcal{M}}_1 = \frac{1}{2} \left(-\xi_{\text{eff}}^{-1/2} + \sqrt{\xi_{\text{eff}}^{-1} - 4} \right) \quad (\text{C9})$$

APPENDIX D: GENERALIZED FAVRE-AVERAGED ANTESONIC CONDITION

Using Equation (C9), we can now solve Equation (B21) for the antesonic condition:

$$\xi_{\text{eff}} = \frac{1}{32} \left(8\Xi_2 + \sqrt{25 - 16\Xi_2} - 5 \right), \quad (\text{D1})$$

which, in the limit $\xi_{\text{cen}} \ll 1$, $\xi_{\text{turb}} \ll 1$, reduces to

$$\xi_{\text{th}} + \frac{1}{3} \xi_{\text{cen}} + \frac{1}{3} \xi_{\text{turb}} = \frac{3}{16}. \quad (\text{D2})$$

This paper has been typeset from a \LaTeX file prepared by the author.